THE JOURNAL OF PHYSICAL CHEMISTRY C
A JOURNAL OF THE AMERICAN CHEMICAL SOCIETY

pubs.acs.org/JPCC

Article

Improvement of Photophysical Properties of $CsPbBr_3$ and Mn^{2+}:$CsPb(Br,Cl)_3$ Perovskite Nanocrystals by Sr^{2+} Doping for White Light-Emitting Diodes

Hurriyet Yuce, Mukunda Mandal, Yenal Yalcinkaya, Denis Andrienko, and Mustafa M. Demir*

Cite This: *J. Phys. Chem. C* 2022, 126, 11277−11284

Read Online

ACCESS | Metrics & More | Article Recommendations | Supporting Information

ABSTRACT: All-inorganic metal halide perovskite nanocrystals (NCs) having the general formula ABX_3, where A is a monovalent cation, for example, Cs^+, B is a divalent cation, typically Pb^{2+}, and X is Cl^-, Br^-, I^-, or their binary mixture, show potential in optoelectronic devices. In this work, we explore the effect of B-site doping on the optoelectronic properties of $CsPbX_3$ NCs (X = Br, Cl). First, the Pb^{2+} ions in the pristine $CsPbBr_3$ NC are partially substituted by Mn^{2+} ions. The alkaline earth metal strontium is then doped on both pristine and the Mn^{2+}-substituted NCs. We found that a small percentage of Sr^{2+} doping remarkably improves the photoluminescence quantum yield of $CsPbBr_3$ and Mn^{2+}-state emission in Mn^{2+}:$CsPb(Br,Cl)_3$ NCs. Perovskite NC film/poly(methyl methacrylate) composites with all four NC variants were used in a white light-emitting diode (WLED), where Sr^{2+} doping increased the luminous efficiency of the WLED by ∼4.7%. We attribute this performance enhancement to a reduced defect density and an attenuated microstrain in the local NC structure.

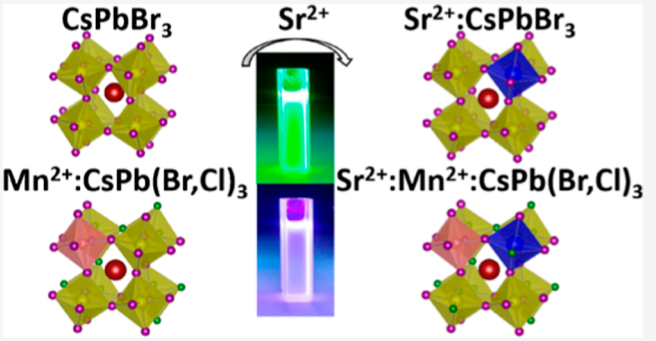

INTRODUCTION

All-inorganic lead halide perovskite nanocrystals (NCs), for example, $CsPbX_3$ (X = Cl^-, Br^-, I^-), have attracted remarkable attention owing to their high photoluminescence quantum yield (PLQY), defect tolerance, adjustable band gaps, narrow PL linewidth, and low-cost fabrication.[1−3] These features make perovskite NCs a good candidate for optoelectronic applications, such as light-emitting diodes (LEDs),[4−6] solar cells,[7,8] lasers,[9,10] and photodetectors.[11,12] In perovskite-based white LEDs (WLEDs), $CsPbX_3$ perovskite NCs can be used as PL converters either by using a combination of red-/green-/blue-emitting perovskites and exciting them using a UV LED[13] or by using the combinations of red-/green-emitting perovskites excited using a blue LED.[14] Conveniently, in $CsPbX_3$ perovskite NCs, the halogen content X^- can be tuned to alter the emission color, for example, the $CsPbI_3$, $CsPbBr_3$, and $CsPbCl_3$ NCs can be deployed as the red (∼1.7 eV), green (∼2.4 eV), and blue (∼3.0 eV) emitters, respectively.[1] However, these perovskite NCs under ambient conditions often suffer from low stability, while the presence of surface defects promotes non-radiative recombinations and deteriorates optical properties.[15,16]

Compositional engineering is a promising method to counter these problems. Homovalent M^{2+} ions (M = Zn,[17,18] Cd,[17,19] Sr,[20,21] Mn,[22,23] and Sn[17,24]) or heterovalent N^{3+} dopants (N = Ce,[25] Bi,[26] Sb,[27] and Al[28]) can increase stability and reduce defect density in perovskite NCs.[16,29,30] Among these dopants, Mn^{2+} incorporation into the $CsPbX_3$ (X = Br, Cl) perovskite lattice gives rise to a characteristic emission around ∼2.1 eV[31] due to the d−d transition between the $^4T1$ and $^6A1$ configurations.[32,33] Therefore, Mn^{2+}:$CsPbX_3$ (X = Br,Cl) perovskite NCs can serve as a viable alternative to $CsPbI_3$ NCs for harnessing emission in the red region in perovskite-based WLEDs,[34−36] given that Mn^{2+}:$CsPbX_3$ (X = Br, Cl) NCs have better phase stability than $CsPbI_3$ NCs.[37] Nevertheless, low PLQY of the Mn state emission is still an issue, which can be improved by co-doping Mn^{2+}:$CsPbX_3$ NCs with bivalent Co^{2+},[38] Ni^{2+},[39] and Cu^{2+}[40] or trivalent Bi^{3+}[41] and Yb^{3+}[42] ions.

In this work, we present improved photophysical properties of $CsPbBr_3$ and Mn^{2+}:$CsPb(Br,Cl)_3$ perovskite NCs achieved by Sr^{2+} doping. We utilized scanning transmission electron microscopy (STEM) to show that Sr^{2+} doping leads to a more uniform size distribution of the perovskite NCs. Microstrain calculations were performed by using the Williamson−Hall (W−H) method extracted from X-ray diffraction (XRD) analyses, which revealed that Sr^{2+} doping decreases defect

Received: February 21, 2022
Revised: June 14, 2022
Published: June 28, 2022

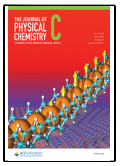

https://doi.org/10.1021/acs.jpcc.2c01244
J. Phys. Chem. C 2022, 126, 11277−11284

Table 1. Actual Sr^{2+}/Pb^{2+} mol Ratio, NC Size, PLQY, and PL Lifetime of Various $CsPbBr_3$ NC Samples Having Different $\%Sr^{2+}$ Dopings

% Sr^{2+} amount in Sr^{2+}:$CsPbBr_3$	Actual Sr^{2+}/Pb^{2+} mol ratio (%)	Average NC Size (nm)	PLQY (%)	PL lifetime (ns)
0% Sr^{2+}		20.3	84.7	7.62
1% Sr^{2+}	0.047	16.8	88.8	8.42
2% Sr^{2+}	0.099	17.3	92.6	10.39
5% Sr^{2+}	0.238	16.0	83.0	7.30
10% Sr^{2+}	1.051	17.0	70.0	6.84

density in the perovskite NCs. Consequently, a remarkable increase in the PLQY with longer PL lifetimes was observed for both Sr^{2+}-doped NCs, Sr^{2+}:$CsPbBr_3$ and Sr^{2+}:Mn^{2+}:$CsPb(Br,Cl)_3$.

Finally, perovskite-based WLEDs were constructed by using $CsPbBr_3$/PMMA [PMMA = poly(methyl methacrylate)] and Mn^{2+}:$CsPb(Br,Cl)_3$/PMMA NCs as PL converters excited using a UV LED. WLEDs fabricated with Sr^{2+}-doped perovskite NCs, that is, Sr^{2+}:$CsPbBr_3$ and Sr^{2+}:Mn^{2+}:$CsPb(Br,Cl)_3$, exhibit a higher PL intensity, higher luminescence efficiency, and slightly higher color rendering index (CRI) than those fabricated with pristine $CsPbBr_3$ and Mn^{2+}:$CsPb(Br,Cl)_3$ perovskite NCs. The results presented here provide a good platform to enhance the photophysical properties of $CsPbBr_3$ and Mn^{2+}:$CsPb(Br,Cl)_3$ perovskite NCs using the Sr^{2+} doping strategy.

EXPERIMENTAL PROCEDURE

Materials. Lead(II) bromide ($PbBr_2$, ≥98%), strontium bromide ($SrBr_2$, 99.99% trace metal basis), manganese(II) chloride tetrahydrate ($MnCl_2{\cdot}4H_2O$, ≥98%), cesium carbonate (Cs_2CO_3, 99.9%, Sigma-Aldrich), 1-octadecene (ODE, 90%), oleylamine (OLAM, 70%), and oleic acid (OA, 90%) were purchased from Sigma-Aldrich. Toluene (≥99%, Merck) was purchased and used without any further purification. PMMA with an average M_w of 15,000 (GPC) was purchased from Aldrich Chemical Company, Inc.

Synthesis of Cs-Oleate for $CsPbBr_3$ NCs. 203.5 mg (266.67 mg) of Cs_2CO_3, 625 μL (1,167 μL) of OA, and 10 mL of ODE were put into a round bottom flask and dried under vacuum at 120 °C while stirring for 1 h. After drying, the temperature was increased to 150 °C under a nitrogen atmosphere. The solution was kept at 150 °C overnight to make sure that all Cs_2CO_3 reacted with OA. The values given in parentheses are for Cs-oleate synthesis of pristine and Sr^{2+}:Mn^{2+}:$CsPb(Br,Cl)_3$ NCs.

Synthesis of Pristine and Sr^{2+}:$CsPbBr_3$ NCs. For the synthesis of pristine $CsPbBr_3$ NCs, first, 17.2 mg of $PbBr_2$ was put into a glass tube along with 1.25 mL of ODE, 125 μL of OA, and 125 μL of OLAM and dissolved/degassed at 120 °C for 30 min under vacuum. After degassing, the temperature was increased to 180 °C under nitrogen, and then, 100 μL of Cs-oleate was injected. After injection, the solution was immediately cooled down using an ice bath and then centrifuged for 15 min at 6000 rpm. Later, the supernatant was discarded, and the NCs were dispersed in toluene. For the synthesis of Sr^{2+}:$CsPbBr_3$ NCs, the same procedure was followed except that 1, 2, 5, and 10% $SrBr_2$ was added to the solution, while the same molar amount of $PbBr_2$ was excluded.

Synthesis of Mn^{2+}:$CsPb(Br,Cl)_3$ and Sr^{2+}:Mn^{2+}:$CsPb(Br,Cl)_3$ NCs. For the synthesis of Mn^{2+}:$CsPb(Br,Cl)_3$ NCs, first, 9.175 mg of $PbBr_2$ and 4.95 mg of $MnCl_2{\cdot}4H_2O$ were put into a glass tube along with 1.25 mL of ODE, 125 μL of OA, and 125 μL of OLAM and dissolved/degassed at 120 °C for 30 min under vacuum. After degassing, the temperature was increased to 180 °C where 100 μL of Cs-oleate was injected under nitrogen. After injection, the solution was immediately cooled down using an ice bath and then centrifuged for 15 min at 6000 rpm. The supernatant was then discarded, and the perovskite NCs were dispersed in toluene. For the synthesis of Sr^{2+}:Mn^{2+}:$CsPb(Br,Cl)_3$ NCs, the same process was followed except that 2% $SrBr_2$ was added to the solution, while the same molar amount of $PbBr_2$ was excluded.

Fabrication of the WLED. 0.5 g of PMMA was dissolved in 10 mL of toluene. For each film of $CsPbBr_3$, drop-cast films were prepared with the mixture of 40 μL of PMMA and 120 μL of the perovskite, while Mn^{2+}:$CsPb(Br,Cl)_3$ drop-cast films were prepared with the mixture of 40 μL of PMMA and 240 μL of perovskite dispersion on 1.5 cm × 1.5 cm glass substrates. Then, these $CsPbBr_3$ and Mn^{2+}:$CsPb(Br,Cl)_3$ (for 0 and 2% Sr^{2+} series, respectively) were placed on the LED laterally. The emission spectra were taken from the perovskite layers excited with UV light (366 nm of wavelength, 12 V, and 8 W power), and the International Commission on Illumination (CIE) chromaticity diagram was extracted from the OSRAM ColorCalculator program.

Characterization. STEM images for all perovskite NCs were taken by using scanning electron microscopy (SEM) with STEM mode: Quanta 250, FEI, Hillsboro, OR. Perovskite dispersions were dropped onto 300 mesh holey carbon-Cu (50 μm) for STEM images. XRD analyses were done by using X'Pert Pro, Philips, Eindhoven, the Netherlands. Optical measurements including absorption, PL, PL lifetime, and PLQY were carried out on an FS5 spectrofluorometer (Edinburgh Instruments, U.K.). For PL and PLQY measurements, excitation wavelengths of $CsPbBr_3$ and Mn^{2+}:$CsPb(Br,Cl)_3$ samples were 400 nm and 390 nm, respectively. For lifetime measurements, $CsPbBr_3$ and Mn^{2+}:$CsPb(Br,Cl)_3$ samples were excited with 442 nm and 307 nm lasers, respectively. Trace metal analysis was carried out using an inductively coupled plasma-mass spectrometer on an Agilent 7500ce Octopole Reaction System.

RESULTS AND DISCUSSION

Inductively coupled plasma mass spectrometry (ICP−MS) measurements were carried out to determine the actual doping ratios of Sr^{2+}/Pb^{2+} in Sr^{2+}-doped Sr^{2+}:$CsPbBr_3$ (Table 1 and Figure S1) and Sr^{2+}:Mn^{2+}:$CsPb(Br,Cl)_3$ NCs (Table S1). The ICP−MS analysis shows that Sr^{2+} was successfully doped into perovskite NCs. The Sr^{2+}/Pb^{2+} ratio was systematically increased by increasing the $SrBr_2$ concentration in the perovskite solution. The Sr^{2+} doping concentrations measured against their addition amounts agreed with the report by Chen et al. on Sr^{2+}:$CsPbI_3$ NCs.[20] Since $MnCl_2$ was used for incorporating Mn^{2+} ions into the pristine $CsPbBr_3$ particle, a fraction of bromide ions were replaced by chloride ions. Ion

https://doi.org/10.1021/acs.jpcc.2c01244
J. Phys. Chem. C 2022, 126, 11277−11284

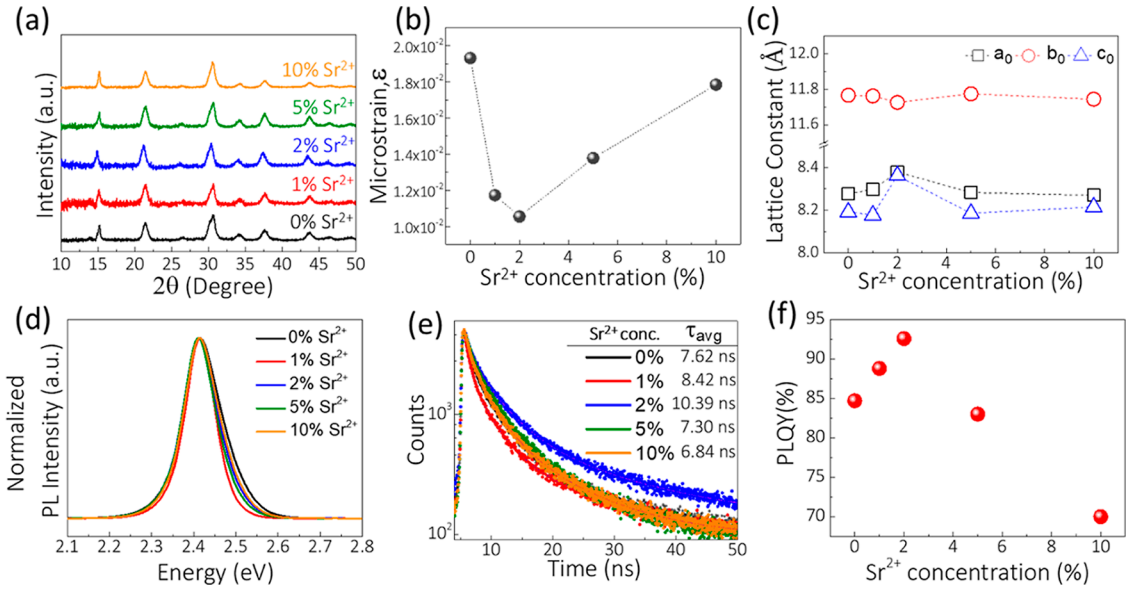

Figure 1. (a) XRD patterns, (b) microstrain values, (c) lattice parameters obtained by the W−H plot, (d) PL spectra, (e) time-resolved PL (TRPL) plot, and (f) PLQY distribution of pristine and Sr^{2+}:$CsPbBr_3$ NCs.

chromatography (IC) analysis revealed Br^-/Cl^- ratios in Mn^{2+}:$CsPb(Br,Cl)_3$ and 2%Sr^{2+}:Mn^{2+}:$CsPb(Br,Cl)_3$ samples to be 72.34 and 75.26%, respectively (Table S1).

The relative propensity for the formation of a given NC was explored computationally employing density functional theory (DFT). We first constructed three cubic NCs of size ∼3 nm (Figure S10). Their cohesive energy ($E_{cohesive}$), which quantifies the energy required to dissociate the atoms constituting the NC into a collection of neutral free atoms, was calculated using eq S5 (see the Supporting Information). For the pristine $CsPbBr_3$, Sr^{2+}-doped Sr^{2+}:$CsPbBr_3$, and Sr^{2+}/Mn^{2+} co-doped Sr^{2+}:Mn^{2+}:$CsPb(Br,Cl)_3$ NCs, $E_{cohesive}$ was computed to be 3.04, 3.05, and 3.17 eV/atom, respectively. Hence, the Sr^{2+} doping replacing two Pb^{2+} ions is marginally favorable ($\Delta E_{cohesive} \sim 0.01$ eV/atom), whereas the Cl^- anions from $MnCl_2$ drive the formation of Sr^{2+}:Mn^{2+}:$CsPb(Br,Cl)_3$, which has $\Delta E_{cohesive} \sim 0.13$ eV/atom when compared with the pristine NC.

Perovskites doped with Mn^{2+} have been reported in the literature to have a marginally increased $E_{cohesive}$[43] and a generally improved robustness.[16,44] Consequently, two additional models were examined to investigate the effects of Mn doping on $E_{cohesive}$, Mn^{2+}:$CsPbBr_3$ and Sr^{2+}:$CsPb(Br,Cl)_3$. In our simulations, however, the calculated $E_{cohesive}$ was not affected by Mn doping. $E_{cohesive}$ was maintained at 3.04 eV/atom in the Mn^{2+}:$CsPbBr_3$ model, which substitutes two Mn^{2+} ions for two Pb^{2+} ions in the pristine NC. $E_{cohesive}$ was again unchanged at 3.17 eV/atom for the Sr^{2+}:$CsPb(Br,Cl)_3$ model, where two Mn^{2+} dopants from the Sr^{2+}:Mn^{2+}:$CsPb(Br,Cl)_3$ particle have been replaced with the original Pb^{2+} ions. Accordingly, Mn^{2+} doping seems to have a less pronounced effect on $E_{cohesive}$, and hence on stability, for bromide nanoparticles than it does for the iodide nanoparticles, for which it is hypothesized that the smaller Mn^{2+} ion partially releases the strain imposed by the larger iodide ions.[16]

The morphology and size distribution of $CsPbBr_3$ NCs upon Sr^{2+} doping were monitored via the STEM mode in SEM. The incorporation of Sr^{2+} ions into the perovskite lattice does not significantly affect the structure and morphology (Figure S2). The reason for the decrease in NC size upon Sr^{2+} doping (Figure S2) could be the effect of the impurity (i.e., the dopant) on crystallization dynamics.[45] We argue that the Sr^{2+} impurities lead to a reduction of the energy threshold for nucleation and cause more nuclei to form, resulting in a smaller NC size. The uniformity of NC size distribution is improved upon Sr^{2+} doping until the 2% Sr^{2+} concentration; however, higher Sr^{2+} concentrations beyond 2% adversely affect NC homogeneity (Figure S2a−e insets).

Figure 1a shows the XRD patterns of pristine and Sr^{2+}:$CsPbBr_3$ NC samples having various Sr^{2+} concentrations. XRD reflections of all samples confirm the orthorhombic *Pnma* crystal structure of $CsPbBr_3$.[46] The incorporation of Sr^{2+} ions into the perovskite lattice does not cause any additional XRD reflection, confirming no phase transition upon doping. Furthermore, due to the similar ionic radii of Pb^{2+} (119 pm) and Sr^{2+} (118 pm) ions,[47] no systematic shift in XRD reflections was observed upon Sr^{2+} doping.

The absence of a systematic shift in the XRD patterns (Figure 1a) motivated us to investigate the influence of the Sr^{2+}-doping concentration on microstrain, which describes local distortions of a crystal lattice.[48,49] Microstrain in the studied NCs was calculated from the slope of the WH plot (Figure S4 and Table S3). Figure 1b shows that microstrain decreases upon Sr^{2+} additive until the 2% concentration and then systematically increases at higher concentrations. This suggests that until the 2% Sr^{2+} concentration, the defect density in the NCs and concomitantly defect-related lattice distortions are reduced, resulting in a smaller microstrain in the crystal structure.

Variation of three cell-length lattice constants (a_0, b_0, and c_0) as a function of the Sr^{2+}concentration is summarized in Table S2, and their trend is shown in Figure 1c. We observe that the b_0 parameter reaches a minimum at the 2% Sr^{2+} concentration and then increases as the Sr^{2+} concentration exceeds 2%, whereas the a_0 and c_0 parameters follow the opposite trend. These results indicate that the octahedral tilt angle changes upon Sr^{2+} doping. Recalling the trend in microstrain with the Sr^{2+}-doping concentration, which reaches a minimum for the

https://doi.org/10.1021/acs.jpcc.2c01244
J. Phys. Chem. C 2022, 126, 11277−11284

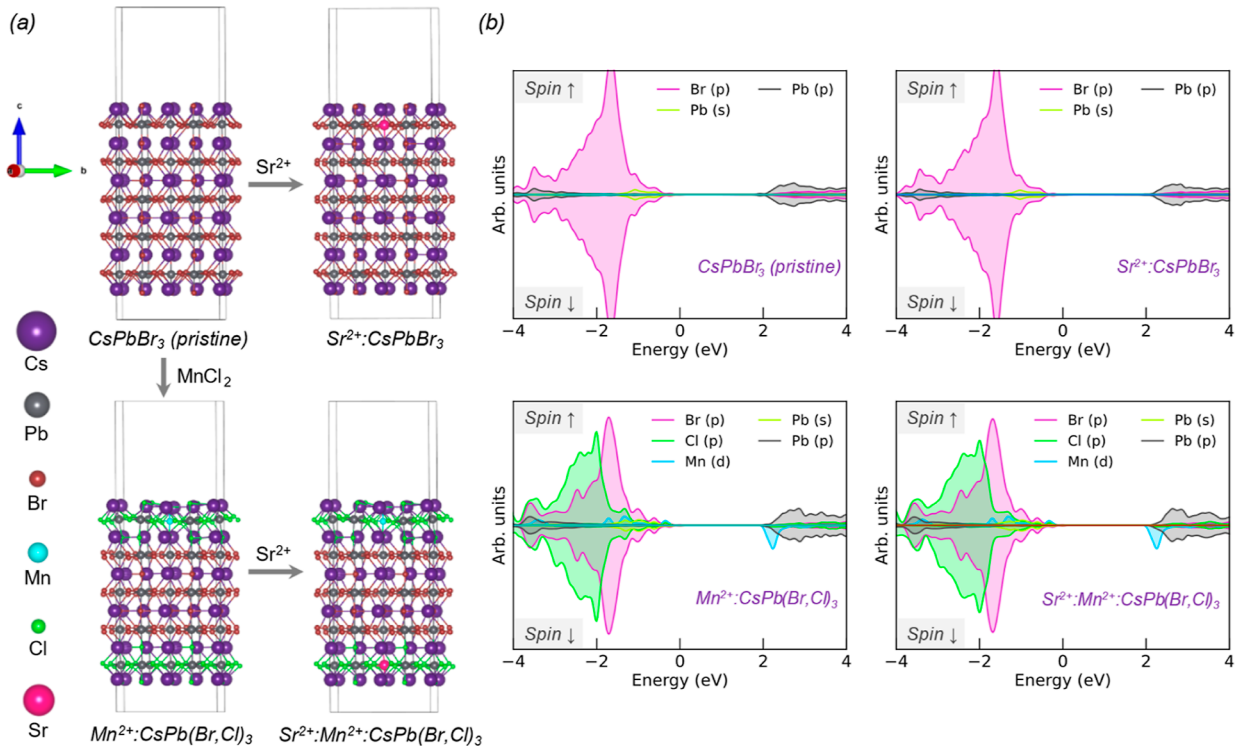

Figure 2. (a) Four periodic slab models considered for the computational study: pristine $CsPbBr_3$, Sr^{2+}-doped Sr^{2+}:$CsPbBr_3$, Mn^{2+}-doped Mn^{2+}:$CsPb(Br,Cl)_3$, and Sr^{2+}/Mn^{2+} co-doped Sr^{2+}:Mn^{2+}:$CsPb(Br,Cl)_3$ and (b) their corresponding pDOS.

2% Sr^{2+} sample, we argue that the reduced defect-related lattice distortions in the perovskite NCs are the reason for the change in lattice parameters, peaking at 2% Sr^{2+}.

To understand the doping effect further, we have carried out optical measurements as shown in Figure 1d–f. The PL spectra of pristine and Sr^{2+}:$CsPbBr_3$ NCs are shown in Figure 1d. Despite the changes in the NC size upon doping (Table 1), the PL emission energy (Figure 1d) and absorption edges (Figure S5) of all samples are strikingly similar. We rationalize this by considering that the studied $CsPbBr_3$ NCs are within the intermediate-to-weak quantum confinement regime,[50] and the incorporation of Sr^{2+} ions into the lattice does not affect the band gap energy of $CsPbBr_3$.

From Tauc's plot (Figure S5), the band gap energies of both pristine $CsPbBr_3$ and Sr^{2+}:$CsPbBr_3$ NC samples are calculated to be ∼2.39 eV. PL signals were centered at 2.41 eV. Furthermore, the full width half-maxima of PL peaks were reduced upon Sr^{2+} doping, in line with the NC size distribution (Figure S2).

To better understand the effect of Sr^{2+} doping on the optoelectronic properties of the NCs, 2D periodic slab models were constructed for the pristine $CsPbBr_3$ and 5% Sr^{2+}-doped Sr^{2+}:$CsPbBr_3$ NCs (Figure 2a, top) and analyzed using DFT. Inspection of the projected densities of states (pDOS; Figure 2b, top) and the band structures (Figure S11) of the pristine and Sr^{2+}-doped models suggests that both NCs are a direct-bandgap material, with the valence band maximum (VBM) and conduction band minimum (CBM) located at the Γ-point. In line with the experimental observations, Figure 2b shows that Sr^{2+} inclusion into $CsPbBr_3$ NCs had no significant effect on the DOS, where the VBM consists mainly of filled Br(p) orbitals, while the CBM is made up mainly of empty Pb(p) orbitals.

Figure 1e shows time-resolved PL (TRPL) results for $CsPbBr_3$ NCs with varied Sr^{2+} contents. The average PL lifetimes (τ_{avg}) of the samples, calculated using eq S4, systematically increase upon the incorporation of Sr^{2+} ions into the perovskite NCs until the 2% concentration. At higher Sr^{2+} concentrations (>2%), however, the PL lifetime gradually decreases (Table 1). Considering that PL lifetimes are inversely proportional to the defect concentration,[51,52] the trend in PL lifetimes agrees with that of the calculated microstrain data. The PLQY results in Figure 1f demonstrate a trend analogous to that of the PL lifetime and microstrain. The PLQY of the pristine $CsPbBr_3$ NC was found to be 84.7%. Sr^{2+} doping increased the PLQY to 88.8% for 1% Sr^{2+} and 92.6% for 2% Sr^{2+}. As Sr^{2+} concentrations increased, PLQY dropped to 83% for 5% Sr^{2+} and then to 70% for 10% Sr^{2+}.

According to the microstrain calculations (Figure 1b), defect-related distortions are reduced when Sr^{2+} ions are incorporated into the $CsPbBr_3$ lattice until the 2% concentration. The minimum microstrain originating from fewer defects was also determined for the same 2% Sr^{2+} sample. Since defect sites serve as potential non-radiative recombination centers for this class of material, the reduced defect density at low Sr^{2+}-doping concentrations should eliminate non-radiative recombination pathways, resulting in a higher PLQY and longer PL lifetime.[53] Beyond 2% Sr^{2+} addition, we argue that the added dopants may trigger the formation of new defects,[21] which would cause an increased microstrain and may lead to a reduction in PL lifetimes and PLQY.

The STEM images of Mn^{2+}:$CsPb(Br,Cl)_3$ and 2% Sr^{2+}:Mn^{2+}:$CsPb(Br,Cl)_3$ NCs are given in Figure S3. 2% Sr^{2+} incorporation into the Mn^{2+}:$CsPb(Br,Cl)_3$ lattice does not change the shape of NCs but decreases the particle size and improves monodispersity, similar to the Sr^{2+}:$CsPbBr_3$ case (Figure S2).

https://doi.org/10.1021/acs.jpcc.2c01244
J. Phys. Chem. C 2022, 126, 11277−11284

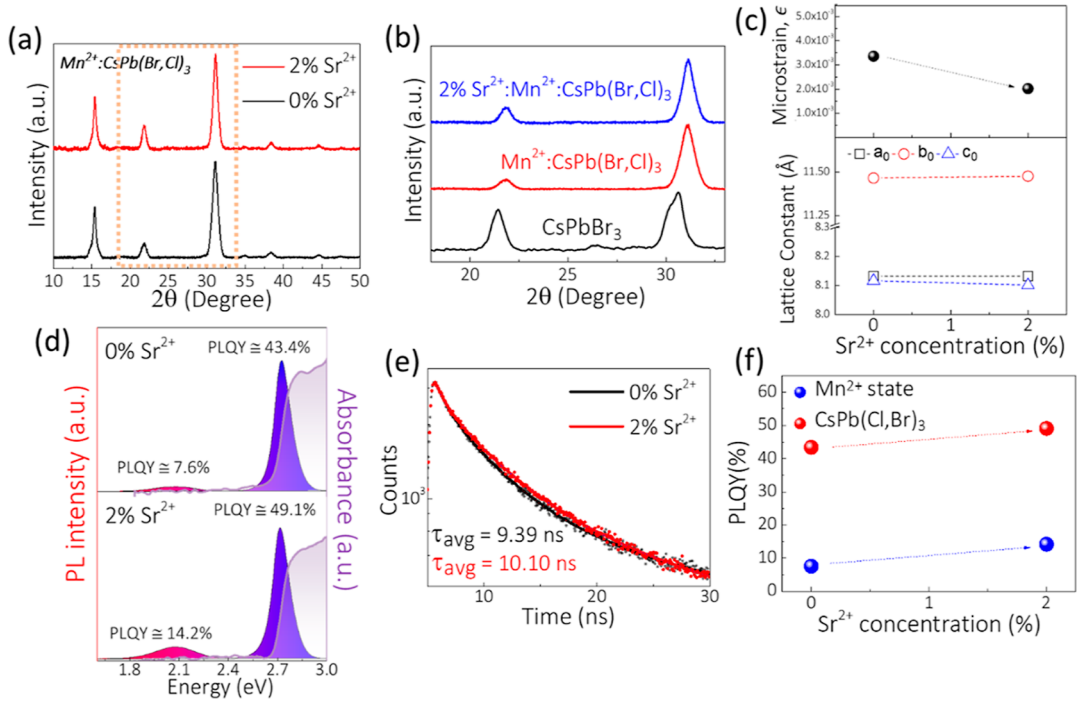

Figure 3. (a) XRD patterns: NCs show reflections at 15.4, 22.0, 31.1, 35.0, 38.4, and 44.6°, (b) comparisons of XRD signal positions for $CsPbBr_3$, Mn^{2+}:$CsPb(Br,Cl)_3$, and Sr^{2+}:Mn^{2+}:$CsPb(Br,Cl)_3$ perovskite NCs, (c) microstrain and lattice constant parameters, (d) PL/absorption spectra, (e) TRPL plot, and (f) PLQY comparisons of Mn^{2+}:$CsPb(Br,Cl)_3$ and 2%Sr^2:Mn^{2+}:$CsPb(Br,Cl)_3$ NCs.

To quantify the impact of the 2% Sr^{2+} additive on the NCs, XRD of Mn^{2+}:$CsPb(Br,Cl)_3$ NCs was carried out. The XRD patterns shown in Figure 3a correspond to the orthorhombic perovskite phase.[54] Since Mn^{2+} ions have a smaller radius (67 pm) than Pb^{2+} ions (119 pm),[47] the XRD signal for Mn^{2+}-doped perovskite NCs shifts to higher angles, indicating that Mn^{2+} ions were successfully incorporated into the perovskite lattice.[55] However, this shift in the XRD signal in Mn^{2+}:$CsPb(Br,Cl)_3$ is not exclusively due to Mn^{2+} ions substituting for Pb^{2+} ions. The overall lattice shrinking can also be attributed to Cl^-/Br^- substitutions (Figure 3b).[37] Subsequent doping of the Sr^{2+} ions into the Mn^{2+}:$CsPb(Br,Cl)_3$ NCs does not cause any peak shift, indicating that the Sr^{2+} ions are substituted with the Pb^{2+} ions instead of the Mn^{2+} ions. Microstrain calculations of both Mn^{2+}:$CsPb(Br,Cl)_3$ and 2%Sr^{2+}:Mn^{2+}:$CsPb(Br,Cl)_3$ samples again confirmed that Sr^{2+} doping reduces microstrain (Figure 3c). Regarding variations in the cell-length lattice constants of the Sr^{2+}/Mn^{2+} co-doped samples, we found that the lattice parameter b_0 increases, while c_0 decreases, and a_0 stays constant at 8.13 Å, as shown in Figure 3c and Table S2.

The UV−vis and PL spectra of the Mn^{2+}:$CsPb(Br,Cl)_3$ and 2%Sr^{2+}:Mn^{2+}:$CsPb(Br,Cl)_3$ samples are shown in Figure 3d, both of which demonstrate very similar absorption behavior. Comparison of these spectra (Figure S6) reveals the appearance of the characteristic PL peak at around 2.1 eV due to the Mn state. Indeed, DFT calculations on both Mn-doped systems reveal (Figure 2b, bottom) Mn *d*-states just below the empty Pb(p) states resulting in a midgap state. Tauc's plots (Figure S7) yield band gaps of 2.70 and 2.69 eV for these two samples, respectively. This slight change in the band gap energies between the samples was also observed in PL peak positions, with the Mn^{2+}:$CsPb(Br,Cl)_3$ and 2% Sr^{2+}:Mn^{2+}:$CsPb(Br,Cl)_3$ NCs exhibiting exciton PL signals at 2.72 and 2.71 eV, respectively (Figure 3d). Considering that Sr^{2+} doping at low concentrations (≤1% actual doping) does not affect the band gap energy (Figure S5), the slight change in band gap and PL emission energies observed herein can be attributed to small differences in Br^-/Cl^- ratios in the perovskite structures; see Table S1.

Interestingly, PL emission due to the Mn state in Mn^{2+}:$CsPb(Br,Cl)_3$ perovskite NCs increases upon Sr^{2+} doping. TRPL measurements of these samples (Figure 3e) reveal that the average PL lifetime of the Mn^{2+}:$CsPb(Br,Cl)_3$ NCs increases from 9.39 to 10.10 ns as a result of the 2% Sr^{2+} additive, attributable to a lower defect density in the 2% Sr^{2+} sample.

PLQY measurements were performed on the Mn^{2+}:$CsPb(Br,Cl)_3$ and 2%Sr^{2+}:Mn^{2+}:$CsPb(Br,Cl)_3$ NCs in the 2.38−1.59 eV (521−780 nm) and 3.02−2.38 eV (410−521 nm) ranges, relevant for the Mn state and perovskite emission, respectively. The PLQY of the Mn-state emission increases from 7.6% in Mn^{2+}:$CsPb(Br,Cl)_3$ to 14.2% in 2% Sr^{2+}:Mn^{2+}:$CsPb(Br,Cl)_3$, as can be seen in Figure 3f, highlighting the beneficial effect of Sr^{2+} co-doping along with Mn^{2+}. In addition, the perovskite PLQY increases from 43.4 to 49.1% due to Sr^{2+} doping. These optical improvements with better exciton-to-Mn^{2+} energy transfer upon Sr^{2+} incorporation are a direct consequence of a lowered defect density.

Finally, two sets of UV-pumped tricolor WLEDs were fabricated using perovskite/PMMA composite films via the drop-casting method (Figures S8 and S9). Under UV light, $CsPbBr_3$/PMMA works as a green emitter, while Mn^{2+}:$CsPb(Br,Cl)_3$/PMMA is a red−blue emitter, and these two combinations were used together to construct the 0% Sr^{2+}:WLED. The 2%Sr^{2+}:WLED, on the other hand, was fabricated using 2%Sr^{2+}:$CsPbBr_3$/PMMA (green emitter) and 2%Sr^{2+}:Mn^{2+}:$CsPb(Br,Cl)_3$/PMMA (red−blue emitter) layers.

https://doi.org/10.1021/acs.jpcc.2c01244
J. Phys. Chem. C 2022, 126, 11277−11284

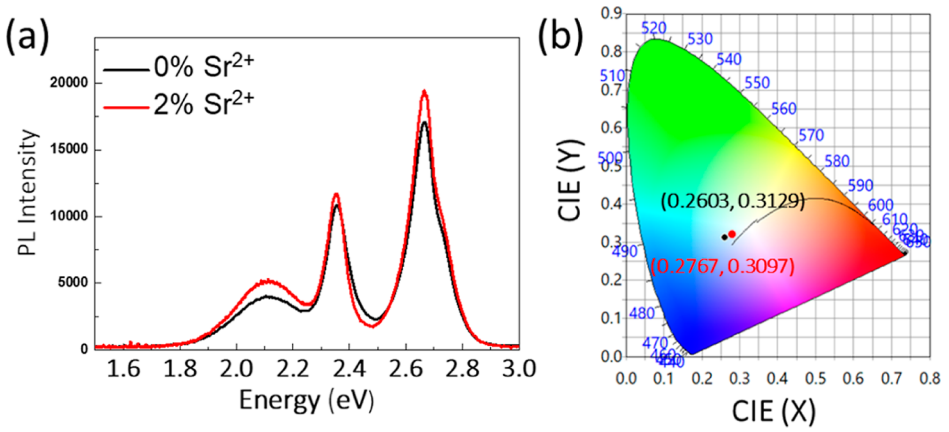

Figure 4. (a) PL spectra of the pristine WLED and 2%Sr^{2+}:WLED and (b) corresponding CIE coordinates.

The PL spectra (Figure 4a) and the CIE coordinates (Figure 4b) of both the 0% and 2%Sr^{2+}:WLED show that the 2% Sr^{2+}:WLED has a higher luminescence efficiency (290 lm/W under a UV light) than the pristine WLED (277 lm/W). Sr^{2+} doping is observed to decrease the computed work function for both pristine and Mn-doped particles (Table 2), which may improve device efficiency and enhance charge extraction in heterojunction-layered devices.[56] Furthermore, the CRI increases from 80 in the pristine 0% Sr^{2+}:WLED system to 83 in the 2% Sr^{2+}:WLED system. We surmise that the deficiency of red emission for the pristine 0% Sr^{2+}:WLED system is partly compensated by the increased PL emission of the Mn state in the Sr^{2+}:WLED system.

Table 2. Computed Work Function and Band Gaps[a] of Four Slab Models (Figure 2a) Considered in This Study[b]

NC particle	work function (eV)	band gap (eV)
$CsPbBr_3$	4.43	1.89 (2.39)
Sr^{2+}:$CsPbBr_3$	4.38	1.98 (2.39)
Mn^{2+}:$CsPb(Br,Cl)_3$	4.28	2.06 (2.70)
Sr^{2+}:Mn^{2+}:$CsPb(Br,Cl)_3$	4.19	2.11 (2.69)

[a]The overestimation of the computed band gap widening upon Sr^{2+} doping can be attributed to possible structural changes when Sr^{2+} is doped since ca 5% Sr^{2+} concentration is used in simulations rather than <1% in experiments. [b]Experimentally obtained band gaps are added in the parenthesis for comparison. The systematic underestimation of the calculated band gaps (with respect to the experiment) can be attributed to the presence of[57] (i) the unphysical electron self-Coulomb repulsion, (ii) derivative discontinuity of the energy with respect to the number of electrons, and (iii) the nonlinear dependence of energy on the number of electrons in the Perdew–Burke–Ernzerhof functional.[58,59]

CONCLUSIONS

We have presented a detailed study on the effect of Sr^{2+} doping into $CsPbBr_3$ and Mn^{2+}:$CsPb(Br,Cl)_3$ perovskite NCs. The STEM images showed a decrease in perovskite NC size after Sr^{2+} doping. The changes in the lattice parameters and microstrains were calculated from XRD signals; microstrain decreased and reached a minimum at the 2% Sr^{2+} concentration, possibly due to the elimination of defects. In addition, the optical properties of the NCs improved, with the PLQY of the $CsPbBr_3$ NCs increasing from 84.7% in the pristine sample to 92.6% in the Sr^{2+}:$CsPbBr_3$ NCs, caused by reduced non-radiative recombination pathways with fewer defects in the sample. Inspired by the optical property enhancements of $CsPbBr_3$ NCs due to Sr^{2+} doping, we have applied the same doping strategy to enhance the optical properties of Mn^{2+}:$CsPb(Br,Cl)_3$ NCs. As a result of 2% Sr^{2+} addition, the PLQY of the Mn^{2+}-state emission increased from 7.6 to 14.2%. Finally, the 2%Sr^{2+}:$CsPbBr_3$ and 2% Sr^{2+}:Mn^{2+}:$CsPb(Br,Cl)_3$ NCs were used to construct a WLED that provided improved white light compared to WLEDs constructed with their undoped counterparts. Our study shows that adding Sr^{2+} to pristine perovskite materials can be a successful strategy for improving their optical properties.

ASSOCIATED CONTENT

Supporting Information

The Supporting Information is available free of charge at https://pubs.acs.org/doi/10.1021/acs.jpcc.2c01244.

STEM images, WH plot calculations, Tauc plots, ICP–MS and IC analysis results, TRPL parameters, and DFT computational details (PDF)

DFT-computed structures: slab models and non-periodic clusters (ZIP)

AUTHOR INFORMATION

Corresponding Author

Mustafa M. Demir – *Department of Materials Science and Engineering, Izmir Institute of Technology, 35430 Izmir, Turkey*; orcid.org/0000-0003-1309-3990; Email: mdemir@iyte.edu.tr

Authors

Hurriyet Yuce – *Department of Materials Science and Engineering, Izmir Institute of Technology, 35430 Izmir, Turkey*

Mukunda Mandal – *Max Planck Institute for Polymer Research, 55128 Mainz, Germany*; orcid.org/0000-0002-5984-465X

Yenal Yalcinkaya – *Max Planck Institute for Polymer Research, 55128 Mainz, Germany*

Denis Andrienko – *Max Planck Institute for Polymer Research, 55128 Mainz, Germany*; orcid.org/0000-0002-1541-1377

Complete contact information is available at: https://pubs.acs.org/10.1021/acs.jpcc.2c01244

Notes

The authors declare no competing financial interest.

■ ACKNOWLEDGMENTS

This work was partially supported by the IZTECH Scientific Research Project with the number 2021IYTE-1-0036. D.A. acknowledges support from the Deutsche Forschungsgemeinschaft (DFG) within the Priority Program SPP2196 ("Perovskite Semiconductors: From Fundamental Properties to Devices") under project no. 424708673. Y.Y. acknowledges the SPP2196 project (Deutsche Forschungsgemeinschaft) for funding. M.M. acknowledges postdoctoral support from the Alexander von Humboldt Foundation.

■ REFERENCES

(1) Protesescu, L.; Yakunin, S.; Bodnarchuk, M. I.; Krieg, F.; Caputo, R.; Hendon, C. H.; Yang, R. X.; Walsh, A.; Kovalenko, M. V. Nanocrystals of Cesium Lead Halide Perovskites ($CsPbX_3$, X = Cl, Br, and I): Novel Optoelectronic Materials Showing Bright Emission with Wide Color Gamut. *Nano Lett.* **2015**, *15*, 3692−3696.

(2) Akkerman, Q. A.; D'Innocenzo, V.; Accornero, S.; Scarpellini, A.; Petrozza, A.; Prato, M.; Manna, L. Tuning the Optical Properties of Cesium Lead Halide Perovskite Nanocrystals by Anion Exchange Reactions. *J. Am. Chem. Soc.* **2015**, *137*, 10276−10281.

(3) Brown, A. A. M.; Damodaran, B.; Jiang, L.; Tey, J. N.; Pu, S. H.; Mathews, N.; Mhaisalkar, S. G. Lead Halide Perovskite Nanocrystals: Room Temperature Syntheses toward Commercial Viability. *Adv. Energy Mater.* **2020**, *10*, 2001349.

(4) Yuan, F.; Ran, C.; Zhang, L.; Dong, H.; Jiao, B.; Hou, X.; Li, J.; Wu, Z. A Cocktail of Multiple Cations in Inorganic Halide Perovskite toward Efficient and Highly Stable Blue Light-Emitting Diodes. *ACS Energy Lett.* **2020**, *5*, 1062−1069.

(5) De Marco, N.; Zhou, H.; Chen, Q.; Sun, P.; Liu, Z.; Meng, L.; Yao, E.-P.; Liu, Y.; Schiffer, A.; Yang, Y. Guanidinium: A Route to Enhanced Carrier Lifetime and Open-Circuit Voltage in Hybrid Perovskite Solar Cells. *Nano Lett.* **2016**, *16*, 1009−1016.

(6) Guner, T.; Demir, M. M. A Review on Halide Perovskites as Color Conversion Layers in White Light Emitting Diode Applications. *Phys. Status Solidi A* **2018**, *215*, 1800120.

(7) Chen, K.; et al. High Efficiency Mesoscopic Solar Cells Using $CsPbI_3$ Perovskite Quantum Dots Enabled by Chemical Interface Engineering. *J. Am. Chem. Soc.* **2020**, *142*, 3775−3783.

(8) Zhang, X.; et al. Inorganic $CsPbI_3$ Perovskite Coating on PbS Quantum Dot for Highly Efficient and Stable Infrared Light Converting Solar Cells. *Adv. Energy Mater.* **2018**, *8*, 1702049.

(9) Yakunin, S.; Protesescu, L.; Krieg, F.; Bodnarchuk, M. I.; Nedelcu, G.; Humer, M.; De Luca, G.; Fiebig, M.; Heiss, W.; Kovalenko, M. V. Low-Threshold Amplified Spontaneous Emission and Lasing from Colloidal Nanocrystals of Caesium Lead Halide Perovskites. *Nat. Commun.* **2015**, *6*, 8056.

(10) Huang, X.; Guo, Q.; Yang, D.; Xiao, X.; Liu, X.; Xia, Z.; Fan, F.; Qiu, J.; Dong, G. Reversible 3D Laser Printing of Perovskite Quantum Dots inside a Transparent Medium. *Nat. Photonics* **2020**, *14*, 82−88.

(11) Bao, C.; Yang, J.; Bai, S.; Xu, W.; Yan, Z.; Xu, Q.; Liu, J.; Zhang, W.; Gao, F. High Performance and Stable All-Inorganic Metal Halide Perovskite-Based Photodetectors for Optical Communication Applications. *Adv. Mater.* **2018**, *30*, 1870288.

(12) Wu, D.; et al. Welding Perovskite Nanowires for Stable, Sensitive, Flexible Photodetectors. *ACS Nano* **2020**, *14*, 2777−2787.

(13) Palazon, F.; Di Stasio, F.; Akkerman, Q. A.; Krahne, R.; Prato, M.; Manna, L. Polymer-Free Films of Inorganic Halide Perovskite Nanocrystals as UV-to-White Color-Conversion Layers in LEDs. *Chem. Mater.* **2016**, *28*, 2902−2906.

(14) Li, X.; Wu, Y.; Zhang, S.; Cai, B.; Gu, Y.; Song, J.; Zeng, H. $CsPbX_3$ Quantum Dots for Lighting and Displays: Roomerature Synthesis, Photoluminescence Superiorities, Underlying Origins and White Light-Emitting Diodes. *Adv. Funct. Mater.* **2016**, *26*, 2435−2445.

(15) Yang, D.; Li, X.; Zhou, W.; Zhang, S.; Meng, C.; Wu, Y.; Wang, Y.; Zeng, H. $CsPbBr_3$ Quantum Dots 2.0: Benzenesulfonic Acid Equivalent Ligand Awakens Complete Purification. *Adv. Mater.* **2019**, *31*, 1970049.

(16) Seth, S.; Ahmed, T.; De, A.; Samanta, A. Tackling the Defects, Stability, and Photoluminescence of $CsPbX_3$ Perovskite Nanocrystals. *ACS Energy Lett.* **2019**, *4*, 1610−1618.

(17) Van der Stam, W.; Geuchies, J. J.; Altantzis, T.; Van Den Bos, K. H. W.; Meeldijk, J. D.; Van Aert, S.; Bals, S.; Vanmaekelbergh, D.; De Mello Donega, C. Highly Emissive Divalent-Ion-Doped Colloidal $CsPb_{1-x}M_xBr_3$ Perovskite Nanocrystals through Cation Exchange. *J. Am. Chem. Soc.* **2017**, *139*, 4087−4097.

(18) Vashishtha, P.; et al. Performance Enhanced Light-Emitting Diodes Fabricated from Nanocrystalline $CsPbBr_3$ with in Situ Zn^{2+} Addition. *ACS Appl. Electron. Mater.* **2020**, *2*, 4002−4011.

(19) Imran, M.; et al. Alloy $CsCd_XPb_{1-X}Br_3$ Perovskite Nanocrystals: The Role of Surface Passivation in Preserving Composition and Blue Emission. *Chem. Mater.* **2020**, *32*, 10641−10652.

(20) Chen, C.; Xuan, T.; Bai, W.; Zhou, T.; Huang, F.; Xie, A.; Wang, L.; Xie, R. J. Highly Stable $CsPbI_3$:Sr^{2+} Nanocrystals with near-Unity Quantum Yield Enabling Perovskite Light-Emitting Diodes with an External Quantum Efficiency of 17.1%. *Nano Energy* **2021**, *85*, 106033.

(21) Lu, M.; Zhang, X.; Zhang, Y.; Guo, J.; Shen, X.; Yu, W. W.; Rogach, A. L. Simultaneous Strontium Doping and Chlorine Surface Passivation Improve Luminescence Intensity and Stability of $CsPbI_3$ Nanocrystals Enabling Efficient Light-Emitting Devices. *Adv. Mater.* **2018**, *30*, No. e1804691.

(22) Liu, W.; Lin, Q.; Li, H.; Wu, K.; Robel, I.; Pietryga, J. M.; Klimov, V. I. Mn^{2+}-Doped Lead Halide Perovskite Nanocrystals with Dual-Color Emission Controlled by Halide Content. *J. Am. Chem. Soc.* **2016**, *138*, 14954−14961.

(23) Parobek, D.; Dong, Y.; Qiao, T.; Son, D. H. Direct Hot-Injection Synthesis of Mn-Doped $CsPbBr_3$ Nanocrystals. *Chem. Mater.* **2018**, *30*, 2939−2944.

(24) Li, M.; Zhang, X.; Matras-Postolek, K.; Chen, H.-S.; Yang, P. An Anion-Driven Sn^{2+} Exchange Reaction in $CsPbBr_3$ Nanocrystals towards Tunable and High Photoluminescence. *J. Mater. Chem. C* **2018**, *6*, 5506−5513.

(25) Yao, J.-S.; et al. Ce^{3+}-Doping to Modulate Photoluminescence Kinetics for Efficient $CsPbBr_3$ Nanocrystals Based Light-Emitting Diodes. *J. Am. Chem. Soc.* **2018**, *140*, 3626−3634.

(26) Begum, R.; Parida, M. R.; Abdelhady, A. L.; Murali, B.; Alyami, N. M.; Ahmed, G. H.; Hedhili, M. N.; Bakr, O. M.; Mohammed, O. F. Engineering Interfacial Charge Transfer in $CsPbBr_3$ Perovskite Nanocrystals by Heterovalent Doping. *J. Am. Chem. Soc.* **2017**, *139*, 731−737.

(27) Zhang, X.; Wang, H.; Hu, Y.; Pei, Y.; Wang, S.; Shi, Z.; Colvin, V. L.; Wang, S.; Zhang, Y.; Yu, W. W. Strong Blue Emission from Sb^{3+}-Doped Super Small $CsPbBr_3$ Nanocrystals. *J. Phys. Chem. Lett.* **2019**, *10*, 1750−1756.

(28) Liu, M.; Zhong, G.; Yin, Y.; Miao, J.; Li, K.; Wang, C.; Xu, X.; Shen, C.; Meng, H. Aluminum-Doped Cesium Lead Bromide Perovskite Nanocrystals with Stable Blue Photoluminescence Used for Display Backlight. *Adv. Sci.* **2017**, *4*, 1700335.

(29) Akkerman, Q. A.; Rainò, G.; Kovalenko, M. V.; Manna, L. Genesis, Challenges and Opportunities for Colloidal Lead Halide Perovskite Nanocrystals. *Nat. Mater.* **2018**, *17*, 394−405.

(30) Ng, C. K.; Wang, C.; Jasieniak, J. J. Synthetic Evolution of Colloidal Metal Halide Perovskite Nanocrystals. *Langmuir* **2019**, *35*, 11609.

(31) Huang, G.; Wang, C.; Xu, S.; Zong, S.; Lu, J.; Wang, Z.; Lu, C.; Cui, Y. Postsynthetic Doping of $MnCl_2$ Molecules into Preformed $CsPbBr_3$ Perovskite Nanocrystals via a Halide Exchange-Driven Cation Exchange. *Adv. Mater.* **2017**, *29*, 1700095.

(32) Pradeep, K. R.; Viswanatha, R. Mechanism of Mn Emission: Energy Transfer vs Charge Transfer Dynamics in Mn-Doped Quantum Dots. *APL Mater.* **2020**, *8*, 020901.
(33) Meinardi, F.; Akkerman, Q. A.; Bruni, F.; Park, S.; Mauri, M.; Dang, Z.; Manna, L.; Brovelli, S. Doped Halide Perovskite Nanocrystals for Reabsorption-Free Luminescent Solar Concentrators. *ACS Energy Lett.* **2017**, *2*, 2368−2377.
(34) Chen, W.; Shi, T.; Du, J.; Zang, Z.; Yao, Z.; Li, M.; Sun, K.; Hu, W.; Leng, Y.; Tang, X. Highly Stable Silica-Wrapped Mn-Doped $CsPbCl_3$ Quantum Dots for Bright White Light-Emitting Devices. *ACS Appl. Interfaces* **2018**, *10*, 43978−43986.
(35) Chen, Z.; et al. Highly Efficient Mn-Doped $CsPb(Br/Cl)_3$ Mixed-Halide Perovskite via a Simple Large-Scale Synthesis Method. *Mater. Sci. Eng. B* **2021**, *273*, 115426.
(36) Zheng, Y.; Yuan, X.; Yang, J.; Li, Q.; Yang, X.; Fan, Y.; Li, H.; Liu, H.; Zhao, J. Cu Doping-Enhanced Emission Efficiency of Mn^{2+} in Cesium Lead Halide Perovskite Nanocrystals for Efficient White Light-Emitting Diodes. *J. Lumin.* **2020**, *227*, 117586.
(37) Protesescu, L.; Yakunin, S.; Bodnarchuk, M. I.; Krieg, F.; Caputo, R.; Hendon, C. H.; Yang, R. X.; Walsh, A.; Kovalenko, M. V. Nanocrystals of Cesium Lead Halide Perovskites ($CsPbX_3$, X = Cl, Br, and I): Novel Optoelectronic Materials Showing Bright Emission with Wide Color Gamut. *Nano Lett.* **2015**, *15*, 3692−3696.
(38) Cao, Z.; Li, J.; Wang, L.; Xing, K.; Yuan, X.; Zhao, J.; Gao, X.; Li, H. Enhancing Luminescence of Intrinsic and Mn Doped $CsPbCl_3$ Perovskite Nanocrystals through Co^{2+} Doping. *Mater. Res. Bull.* **2020**, *121*, 110608.
(39) Xing, K.; Yuan, X.; Wang, Y.; Li, J.; Wang, Y.; Fan, Y.; Yuan, L.; Li, K.; Wu, Z.; Li, H.; Zhao, J. Improved Doping and Emission Efficiencies of Mn-Doped $CsPbCl_3$ Perovskite Nanocrystals via Nickel Chloride. *J. Phys. Chem. Lett.* **2019**, *10*, 4177−4184.
(40) Zhang, J.; Zheng, Y.; Liu, G.; Ma, Y.; Gong, L.; Guan, R.; Cui, X.; Yan, J.; Zhao, J.; Yang, J. Pressure-Engineered Optical and Charge Transport Properties of Mn^{2+}/Cu^{2+} Codoped $CsPbCl_3$ Perovskite Nanocrystals via Structural Progression. *ACS Appl. Mater. Interfaces* **2020**, *12*, 48225−48236.
(41) Shao, H.; Bai, X.; Cui, H.; Pan, G.; Jing, P.; Qu, S.; Zhu, J.; Zhai, Y.; Dong, B.; Song, H. White Light Emission in Bi^{3+}/Mn^{2+} Ion Co-Doped $CsPbCl_3$ Perovskite Nanocrystals. *Nanoscale* **2018**, *10*, 1023−1029.
(42) Cai, T.; Wang, J.; Li, W.; Hills-Kimball, K.; Yang, H.; Nagaoka, Y.; Yuan, Y.; Zia, R.; Chen, O. Mn^{2+}/Yb^{3+} Codoped $CsPbCl_3$ Perovskite Nanocrystals with Triple-Wavelength Emission for Luminescent Solar Concentrators. *Adv. Sci.* **2020**, *7*, 2001317.
(43) Akkerman, Q. A.; Meggiolaro, D.; Dang, Z.; De Angelis, F.; Manna, L. Fluorescent Alloy $CsPb_xMn_{1-X}I_3$ Perovskite Nanocrystals with High Structural and Optical Stability. *ACS Energy Lett.* **2017**, *2*, 2183−2186.
(44) Wang, Y.; Chen, Y.; Zhang, T.; Wang, X.; Zhao, Y. Chemically Stable Black Phase $CsPbI_3$ Inorganic Perovskites for High-Efficiency Photovoltaics. *Adv. Mater.* **2020**, *32*, 2001025.
(45) Thanh, N. T. K.; Maclean, N.; Mahiddine, S. Mechanisms of Nucleation and Growth of Nanoparticles in Solution. *Chem. Rev.* **2014**, *114*, 7610−7630.
(46) Stoumpos, C. C.; et al. Crystal Growth of the Perovskite Semiconductor $CsPbBr_3$: A New Material for High-Energy Radiation Detection. *Cryst. Growth Des.* **2013**, *13*, 2722−2727.
(47) Shannon, R. D. Revised Effective Ionic Radii and Systematic Studies of Interatomic Distances in Halides and Chalcogenides. *Acta Crystallogr., Sect. A* **1976**, *32*, 751−767.
(48) Wang, X.; Xu, Z.; Zhuo, S.; Hu, P.; Yang, Y.; Zhou, B.; Zhang, W.-H. Strain Modulation for High Brightness Blue Luminescence of Pr^{3+}-Doped Perovskite Nanocrystals via Siloxane Passivation. *ACS Appl. Electron. Mater.* **2021**, *3*, 3815−3823.
(49) Yuce, H.; et al. Understanding the Impact of SrI_2 Additive on the Properties of Sn-Based Halide Perovskites. *Opt. Mater.* **2021**, *123*, 111806.
(50) Becker, M. A.; et al. Bright Triplet Excitons in Caesium Lead Halide Perovskites. *Nature* **2018**, *553*, 189−193.
(51) Ahmed, G. H.; El-Demellawi, J. K.; Yin, J.; Pan, J.; Velusamy, D. B.; Hedhili, M. N.; Alarousu, E.; Bakr, O. M.; Alshareef, H. N.; Mohammed, O. F. Giant Photoluminescence Enhancement in $CsPbCl_3$ Perovskite Nanocrystals by Simultaneous Dual-Surface Passivation. *ACS Energy Lett.* **2018**, *3*, 2301−2307.
(52) Ahmed, T.; Seth, S.; Samanta, A. Boosting the Photoluminescence of $CsPbX_3$ (X = Cl, Br, I) Perovskite Nanocrystals Covering a Wide Wavelength Range by Postsynthetic Treatment with Tetrafluoroborate Salts. *Chem. Mater.* **2018**, *30*, 3633−3637.
(53) Bohn, B. J.; et al. Boosting Tunable Blue Luminescence of Halide Perovskite Nanoplatelets through Postsynthetic Surface Trap Repair. *Nano Lett.* **2018**, *18*, 5231−5238.
(54) Parobek, D.; Roman, B. J.; Dong, Y.; Jin, H.; Lee, E.; Sheldon, M.; Son, D. H. Exciton-to-Dopant Energy Transfer in Mn-Doped Cesium Lead Halide Perovskite Nanocrystals. *Nano Lett.* **2016**, *16*, 7376−7380.
(55) Li, F.; Xia, Z.; Gong, Y.; Gu, L.; Liu, Q. Optical Properties of Mn^{2+} Doped Cesium Lead Halide Perovskite Nanocrystals via a Cation-Anion Co-Substitution Exchange Reaction. *J. Mater. Chem. C* **2017**, *5*, 9281.
(56) Canil, L.; et al. Tuning Halide Perovskite Energy Levels. *Energy Environ. Sci.* **2021**, *14*, 1429−1438.
(57) Crowley, J. M.; Tahir-Kheli, J.; Goddard, W. A. Accurate Ab Initio Quantum Mechanics Simulations of Bi_2Se_3 and Bi_2Te_3 Topological Insulator Surfaces. *J. Phys. Chem. Lett.* **2015**, *6*, 3792−3796.
(58) Perdew, J. P.; Levy, M. Physical Content of the Exact Kohn-Sham Orbital Energies: Band Gaps and Derivative Discontinuities. *Phys. Rev. Lett.* **1983**, *51*, 1884.
(59) Mori-Sánchez, P.; Cohen, A. J.; Yang, W. Localization and Delocalization Errors in Density Functional Theory and Implications for Band-Gap Prediction. *Phys. Rev. Lett.* **2008**, *100*, 146401.

https://doi.org/10.1021/acs.jpcc.2c01244
J. Phys. Chem. C 2022, 126, 11277−11284